Partially replacing Pb^{2+} by Mn^{2+} in hybrid metal halide perovskites

Structural and electronic properties

Bartesaghi, Davide; Ray, Aniruddha; Jiang, Junke; Bouwer, Ricardo K.M.; Tao, Shuxia; Savenije, Tom J.

Important note
To cite this publication, please use the final published version (if applicable).
Please check the document version above.

Partially replacing Pb^{2+} by Mn^{2+} in hybrid metal halide perovskites: Structural and electronic properties

Davide Bartesaghi, Aniruddha Ray, Junke Jiang, Ricardo K. M. Bouwer, Shuxia Tao, and Tom J. Savenije

---

Articles you may be interested in

Partially replacing Pb²⁺ by Mn²⁺ in hybrid metal halide perovskites: Structural and electronic properties

Davide Bartesaghi,[1,2,a] Aniruddha Ray,[1] Junke Jiang,[3]
Ricardo K. M. Bouwer,[4] Shuxia Tao,[3] and Tom J. Savenije[1,a]

[1]*Department of Chemical Engineering, Delft University of Technology,*
2629 HZ Delft, The Netherlands
[2]*Materials Innovation Institute (M2i), 2628 CD Delft, The Netherlands*
[3]*Center for Computational Energy Research, Department of Applied Physics,*
Eindhoven University of Technology, 5600 MB Eindhoven, The Netherlands
[4]*Tata Steel, Research and Development, IJmuiden Technology Centre, P.O. Box 10.000,*
1970 CA IJmuiden, The Netherlands

Tailoring the physical properties of hybrid lead metal halide $APbX_3$ perovskites by means of compositional engineering is one of the key factors contributing to the development of highly efficient and stable perovskite solar cells. While the beneficial effects of partial ionic replacement at the A- and X-sites are largely demonstrated, partial replacement of Pb^{2+} is less explored. Here, we developed a solution-based procedure to prepare thin films of mixed-metal $MAPb_{1-a}Mn_aI_3$ perovskites. Although Mn^{2+} ions have a size that can potentially fit in the B-sites of $MAPbI_3$, using a combination of structural and chemical analysis, we show that only less than 10% of Pb^{2+} can be replaced by Mn^{2+}. A 3% replacement of Pb^{2+} by Mn^{2+} leads to an elongation of the charge carrier lifetimes as concluded from time-resolved PL measurements. However, by analysis of the time-resolved microwave conductance data, we show that the charge carrier mobilities are largely unbalanced, which is in accordance with density functional theory (DFT) calculations indicating that the effective mass of the hole is much higher than that of the electron. Increasing the concentration of Mn^{2+} in the precursor solution above 10% results in formation of amorphous Mn-rich domains in the film, while the perovskite lattice becomes depleted of Mn^{2+}. These domains negatively affect the charge carrier mobilities and shorten the lifetime of photogenerated carriers. The resulting reduction in charge carrier diffusion lengths will severely limit the photovoltaic properties of solar cells prepared from these mixed metal halide perovskites. © *2018 Author(s). All article content, except where otherwise noted, is licensed under a Creative Commons Attribution (CC BY) license (http://creativecommons.org/licenses/by/4.0/).* https://doi.org/10.1063/1.5060953

The extraordinarily rapid rise in the power conversion efficiency of metal halide perovskite solar cells (PSCs)[1,2] has in the last years been accompanied by improvements in their stability.[3] While the first breakthroughs in the field of PSCs were due to changes in the device architecture[4,5] and processing conditions,[6] compositional engineering of the perovskite ABX_3 crystal structure has recently played a crucial role in the achievement of highly stable and efficient PSCs.[7] It has been shown that the properties of hybrid halide perovskites can be tailored and optimized by (partially) replacing the ions at the A-sites and X-sites of the perovskite lattice,[7–9] and the most efficient PSCs are currently realized using mixed-cation, mixed-halide perovskites.[10] By contrast, blending the divalent metal cations at the B-sites to obtain mixed-metal perovskites is a relatively less explored path. Most of the efforts in this direction involved the partial replacement of Pb^{2+} with Sn^{2+} and were initially motivated by the necessity of mitigating the toxicity of lead.[11–14] $MAPb_{1-a}Sn_aX_3$ perovskites (where

---

[a]Authors to whom correspondence should be addressed: d.bartesaghi@tudelft.nl and t.j.savenije@tudelft.nl

MA = CH_3NH_3 and X = I, Br, or Cl) have been synthesized for the full compositional range $0 \leq a \leq 1$[11] and used in photovoltaic devices with efficiencies as high as 17.6%,[15] although the ease with which Sn^{2+} oxidizes to Sn^{4+} severely limits the processing of this class of perovskites.[16,17] Recently, Klug and co-workers demonstrated that partial replacement of lead is possible using transition or alkaline earth metals.[18] In those cases, the photovoltaic performance significantly dropped if more than a few atomic percent of lead was replaced. Very recently, positive effects on the stability and performance were reported on replacing 3% of the Pb^{2+} by Zn^{2+}, Mn^{2+}, or Ni^{2+}.[19]

In this paper, we investigate how partial replacement of Pb^{2+} with Mn^{2+} affects the optoelectronic properties of $MAPbI_3$. Manganese is one of the most abundant metals in the Earth's crust and has a low toxicity.[20] Besides the possibility of using the mixed metal perovskite $MAPb_{1-a}Mn_aI_3$ in photovoltaic devices,[18,19,21] its magnetic properties can be used in low-power, light-controlling applications such as magneto-optical data storage devices.[22] Recently, partial replacement of Pb^{2+} with Mn^{2+} has been demonstrated for lead halide perovskite nanocrystals and nanoplatelets.[23–25]

We prepared thin films of $MAPb_{1-a}Mn_aI_3$ from solution, and we characterized the chemical composition, crystal structure, and optoelectronic properties. Although the elemental analysis confirms the presence of Mn^{2+} and the material retains the perovskite crystal structure even up to 50% replacement, we demonstrate that only less than 10% of Pb^{2+} can be replaced by Mn^{2+} at the B-sites. The excess manganese is located in amorphous, Mn-rich domains.

We characterized the optoelectronic properties of the mixed metal perovskite thin films by means of UV-vis absorption spectroscopy, time-resolved photoluminescence (TRPL), and time-resolved microwave conductance (TRMC). If less than 10% of Pb^{2+} is replaced by Mn^{2+}, charge carrier lifetimes increase; however, the charge transport becomes largely unbalanced: The mobility of holes is more than one order of magnitude lower than the mobility of electrons, which is in accordance with density functional theory (DFT) calculations revealing the effective masses. Segregation of Mn^{2+} in domains outside the perovskite crystals restores balanced transport; however, the mobilities are significantly lower and the recombination rate is faster than in $MAPbI_3$.

Details regarding the experiments are summarised below. Equimolar amounts of hydroiodic acid (HI, 57 vol% in water) and methylamine (CH_3NH_2, 33 wt. % in ethanol) were added in a round-bottom flask and let to react for 2 h in an ice bath while stirring. The precipitate of the solution was collected by rotary evaporation at 50 °C, then washed with diethyl ether, and dried at 60 °C in a vacuum oven for at least 24 h before use.

MAI, $PbAc_2$, and $MnCl_2$ were dissolved in dimethylformamide (DMF) inside of a nitrogen-filled glovebox. Various solutions with different $PbAc_2$:$MnCl_2$ molar ratios have been prepared, keeping the molar ratio of MAI to the total concentration of inorganic salt constant (3:1). The solutions were heated on a hot plate at 70 °C and magnetically stirred for 1 h. Subsequently, the solutions were allowed to cool down to room temperature and filtered (polypropylene filters, 0.45 μm) before use.

Samples for XRD, UV-vis absorption, TRPL, and TRMC measurements have been deposited on quartz substrates; samples for SEM and EDX have been deposited on FTO-coated glass substrates. The quartz substrates were cleaned by O_2 plasma; for FTO-coated glass substrates, a thorough cleaning by using an ultrasonic bath in acetone and isopropanol has been performed prior to O_2 plasma cleaning. The cleaned samples have been transferred in the glovebox, and perovskite films have been deposited on them by spin coating (2000 RPM, 2000 RPM/s, 45 s). The deposited films were annealed at 100 °C (15 min for $MAPbI_3$ films, 2 h for films containing Mn^{2+}) with a thickness of about 200 nm.

XRD measurements were performed using a Bruker D8 Advance diffractometer in the Bragg-Brentano geometry. The monochromatic Co Kα X-ray source was operated at 40 kV and 40 mA.

The fraction of absorbed light was measured with a Perkin-Elmer UV/VIS/NIR Lambda 1050S spectrometer containing a 150 mm Spectralon integrating sphere. The perovskite thin films were measured in the wavelength range 400–850 nm.

TRPL measurements were carried out using an Edinburgh LifeSpec spectrometer equipped with a single-photon counter. The perovskite films were excited at 405 nm with a picosecond pulsed diode laser. A high pass filter was used to prevent photons with wavelength below 450 nm to reach the detector. PL emission spectra of all samples were measured in the range 650–850 nm. PL lifetimes were recorded at the maximum emission wavelength.

Samples were sealed in a microwave cavity within a nitrogen-filled glovebox. The fraction of absorbed microwave (frequency ca. 8.5 GHz) power ($\Delta P/P$) was measured after pulsed optical excitation (repetition rate 10 Hz, $\lambda = 550$ nm). The rise of $\Delta P/P$ is limited by the width of the laser pulses (3.5 ns) and by the response time of the microwave cavity (18 ns). A series of neutral density filters was used to perform light-intensity dependent TRMC measurements.

Top-view SEM secondary electron images were taken with a JEOL-JSM-610LA microscope using 10 kV voltage energy, 10 mm working distance, and ×3000 magnification. Backscattered electron images were taken using 20 kV voltage, 10 mm working distance, and ×200 magnification.

EDX elemental maps and point analysis were carried out using the EDX detector of the JEOL-JSM-610LA microscope, with settings of 20 kV voltage, 10 mm working distance, and ×200 magnification.

The structural optimization of $MAPbI_3$, $MAPb_{0.9375}Mn_{0.0625}I_3$, and $MAPb_{0.875}Mn_{0.125}I_3$ using 12 (unit cell), 192, and 96 atoms (super cells) was performed using DFT within the Perdew, Burke, and Ernzerhof (PBE)[26] functional implemented in the Vienna *ab initio* simulation package (VASP).[27,28] The outermost s, p, and d (in the case of Pb and Mn) electrons are treated as valence electrons whose interactions with the remaining ions are modeled by pseudopotentials generated within the projector-augmented wave (PAW) method.[29,30] An energy cutoff of 500 eV and $6 \times 6 \times 6$, $2 \times 3 \times 3$, and $3 \times 3 \times 3$ k-point meshes were used to achieve energy and force convergence of 0.1 meV and 2 meV/Å for 12, 192, and 96 atoms cells, respectively. The spin-orbit coupling effect was taken into account for the band structure calculations.

Recently, the lead-free compound methylammonium manganese iodide ($MAMnI_3$) has been synthesized and characterized; such a compound is amorphous and does not form a cubic perovskite structure.[31] We started our study by investigating how much Pb^{2+} can be replaced by Mn^{2+} before disrupting the perovskite crystal structure. The most commonly used predictor for the perovskite phase is the Goldschmidt tolerance factor,[32]

$$t = \frac{r_A + r_X}{\sqrt{2}(r_B + r_X)}, \tag{1}$$

where r_A, r_B, and r_X are the ionic radii of monovalent cation (A), divalent cation (B), and halogen anion (X), respectively [Fig. 1(a)]. It has been empirically observed that the perovskite structure can be formed if the tolerance factor is in the range $0.875 < t < 1.06$.[33] Besides the tolerance factor, the octahedral factor is used to assess if the divalent cation B has the right size to fit in the X_6 octahedron,[34]

$$\mu = \frac{r_B}{r_X}. \tag{2}$$

If $\mu < 0.41$, the BX_6 octahedra cannot form, which excludes the formation of the perovskite structure.[34] By combining the perovskite formation criteria for t and μ, one can define a perovskite formation
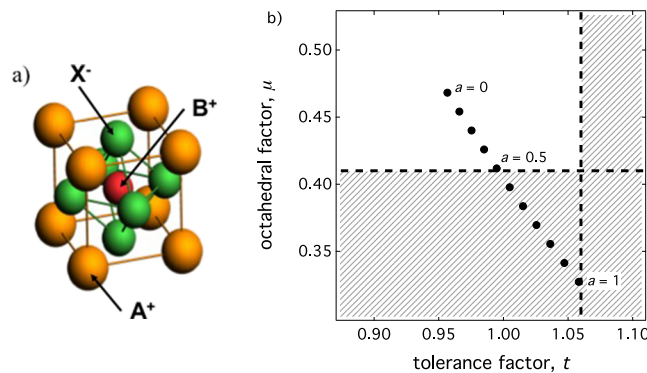

FIG. 1. (a) Crystal structure of ABX_3 perovskite materials; (b) t-μ structure map for $MAPb_{1-a}Mn_aI_3$. The black circles represent t-μ combinations calculated for different values of a. The shaded area indicates the region in which the perovskite structure does not form. The cationic and anionic radii for the calculation of t and μ have been taken from Ref. 33.

region on the t-μ structure map [Fig. 1(b)]. We calculated t and μ for $MAPb_{1-a}Mn_aI_3$ with $0 < a < 1$; for the mixed-metal compounds, we approximated the radius of the divalent cation as the weighted average of the cationic radius of Pb^{2+} (r_{Pb}) and of Mn^{2+} (r_{Mn}),

$$r_B = ar_{Mn} + (1-a)r_{Pb}. \tag{3}$$

For each composition considered, a point is placed on the t-μ structure map in Fig. 1(b). The replacement of Pb^{2+} with the smaller Mn^{2+} cations results in a reduction in μ, which drops below the empirical limit for $a > 0.5$.

The above analysis suggests that it is thus possible to replace half of the Pb^{2+} with Mn^{2+} without disrupting the perovskite structure. To verify this prediction, we prepared mixed-metal compounds using a one-step solution process: methylammonium iodide (MAI), lead acetate ($PbAc_2$), and manganese chloride ($MnCl_2$) were dissolved in DMF and subsequently spin cast to form thin films. The molar ratio of MAI to the total amount of inorganic salt content was kept constant at 3:1. We define the amount of Mn^{2+} in the precursor solution (a_{sol}) as the percentage of $MnCl_2$ with respect to the total amount of bivalent metal salts,

$$a_{sol} = \frac{n_{MnCl_2}}{n_{MnCl_2} + n_{PbAc_2}} \times 100\%, \tag{4}$$

where n_i is the number of moles of the salt i in the precursor solution. For the remaining part of this paper, a film with $a_{sol} = 10\%$ denotes a film that is prepared from a precursor solution with a fraction Mn^{2+} of 0.1.

After spin casting the films, the elemental composition was measured by means of energy-dispersive X-ray spectroscopy (EDX). Quantitative analysis of the data provides the atomic fraction of each element in the sample (Table SI in the supplementary material); the percentage of Mn^{2+} with respect to the total amount of bivalent metals is given by

$$a_{film} = \frac{f_{Mn}}{f_{Mn} + f_{Pb}} \times 100\%, \tag{5}$$

where f_i is the atomic fraction of the element i in the film.

Except for the film with $a_{sol} = 50\%$, all percentages found for a_{film} are somewhat smaller than those for a_{sol} (see Table I). Moreover, from the backscattered electron images and elemental mapping of Mn (Fig. S1), it is evident that for films with $a_{sol} > 30\%$, the films are not uniform and that the lateral distributions of Pb and Mn are not homogenous.

Although elemental analysis confirms the presence of Mn^2 in the films (with roughly the same fraction as in the precursor solutions), this does not imply whether Mn^{2+} ions occupy the B-sites of the perovskite lattice. The X-ray diffraction (XRD) patterns for films with different concentrations of Mn^{2+} are shown in Fig. 2(a). The diffraction pattern of the Mn-free film presents the characteristic peaks of $MAPbI_3$.[35] We note here that the (110) peaks of our samples are located at $2\vartheta \approx 16.35°$, in contrast to the more frequently reported value of $2\vartheta \approx 14.20°$. The discrepancy is due to the Co Kα X-ray source used in our experiment, which emits X-ray at longer wavelengths than the more commonly used Cu Kα source. Interestingly, independent of the values of a_{sol}, the perovskite structure is preserved. Replacement of Pb^{2+} ions with the smaller Mn^{2+} ions is expected to cause a reduction of the perovskite lattice, resulting in a shift of the XRD reflections toward larger angles. For samples

TABLE I. Comparison of the Mn^{2+} fraction in the precursor solutions (a_{sol}) with that in the films (a_{film}).

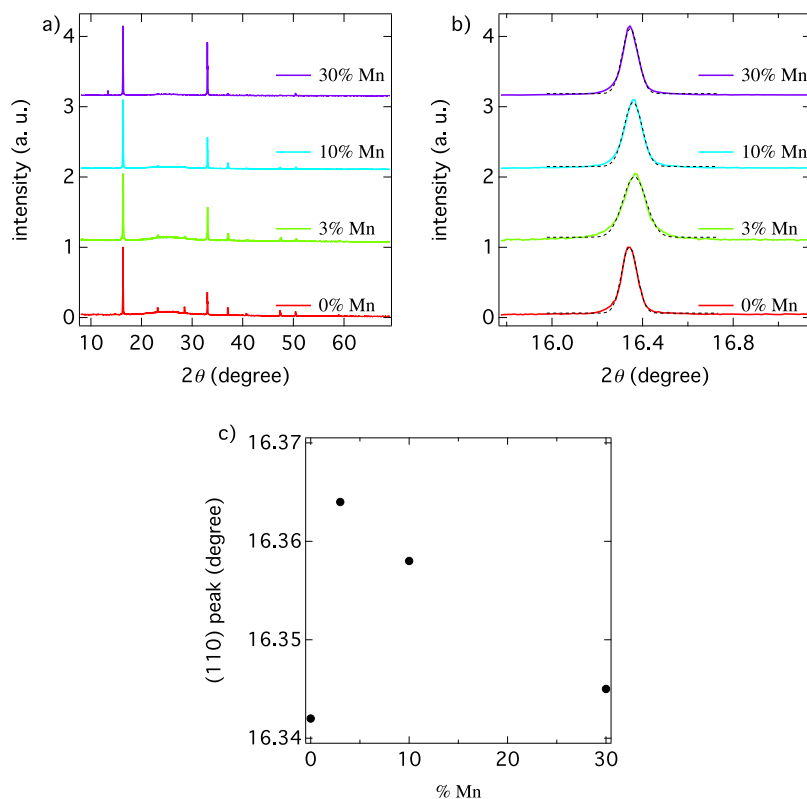| a_{sol} (%)	a_{film} (%)
0	0
10	8.93
20	16.44
30	19.56
40	31.41
50	51.86

FIG. 2. (a) XRD patterns (Co Kα radiation, λ = 1.79 Å) of mixed-metal perovskite films prepared from solutions containing various concentrations of $MnCl_2$ as indicated by the percentage; (b) local region of the XRD patterns around the strongest cubic diffraction peak (110). The dashed lines represent Gaussian fits of the peaks; (c) 2ϑ value of the (110) peak centers as a function of the percentage $MnCl_2$ in the precursor solution.

with a low content of Mn, the (110) peak indeed shifts toward larger 2ϑ [Figs. 2(b) and 2(c)], which is in agreement with the recent literature.[19] Remarkably, the shift is not monotonously increasing with higher Mn concentrations. Instead, for films with $a_{sol} > 3\%$, the (110) peak shifts back toward the position of the (110) peak of $MAPbI_3$. We explain this as follows: while limited amounts of $MnCl_2$ in the precursor solution results in the replacement of Pb^{2+} with Mn^{2+} at the B-sites of the lattice, larger concentrations of $MnCl_2$ yield the formation of Mn-rich domains, depleting the perovskite lattice with Mn^{2+}. Hence, the XRD pattern reverts back to that of $MAPbI_3$. We can also rule out the formation of Mn^{2+} interstitials as this should result in an expansion of the perovskite lattice and consequently a shift of the XRD peaks toward lower angles, as recently observed by Bai and co-workers for Mn-alloying of $CsPbI_2Br$.[36] However, we do not observe any expansion of the $MAPbI_3$ lattice even at the highest Mn^{2+} concentrations (Table SII of the supplementary material).

When a_{sol} exceeds 30%, new features appear in the XRD patterns (Fig. S2). These findings agree with the SEM images of these films (Fig. S1), showing the appearance of new, non-amorphous phases (particularly evident for $a_{sol} = 40\%$ and 50%). Therefore, we decided to not further investigate films with $a_{sol} > 30\%$.

For films with $a_{sol} = 30\%$, presence of Cl is detected by means of EDX (Table SI). Similarly as discussed above for Mn^{2+}, we would expect a shift of the XRD peaks toward larger angles if Cl^- replaced the larger I^- ions in the perovskite structure; the absence of such a shift indicates that Cl^- is also segregated in Mn-rich domains.

Figure 3(a) shows the absorptance measured for thin films of mixed-metal perovskite. The absorption onset does not shift significantly on increasing the Mn^{2+} percentage, indicating that the bandgap of $MAPbI_3$ is virtually unaffected by the presence of Mn^{2+}. The fact that the optical absorption is not significantly modified by the presence of Mn-rich domains implies that these
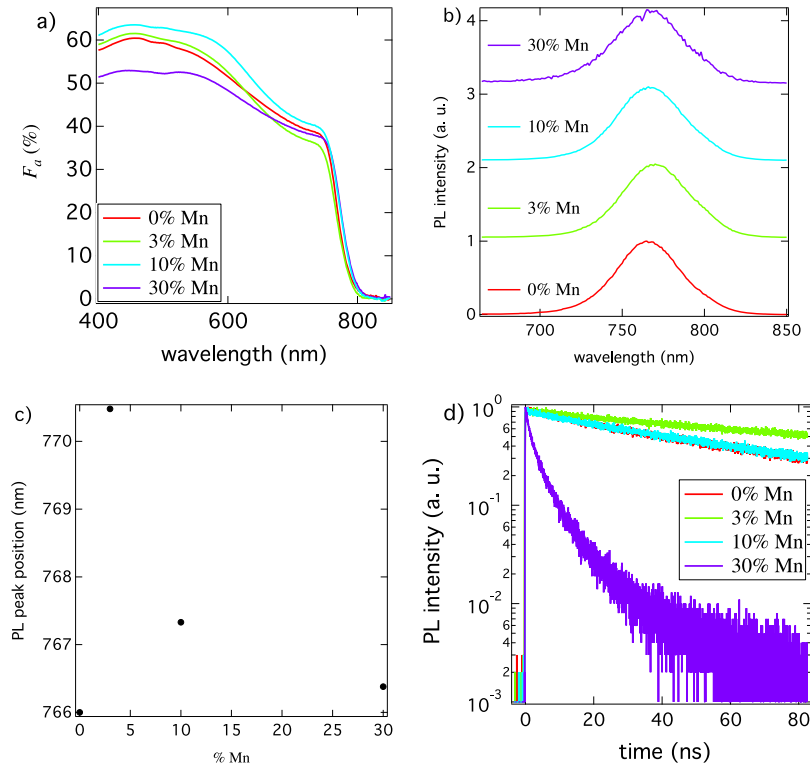
FIG. 3. (a) Absorptance of thin mixed-metal perovskite films prepared from solutions containing various concentrations of $MnCl_2$; (b) normalized PL spectra measured on optical excitation at 405 nm; (c) position of the PL peak vs $MnCl_2$ percentage; (d) TRPL traces measured at the wavelength at which the PL is maximum.

have a large bandgap. Careful analysis of the PL emission spectra presents a small red-shift of the PL peak position [Fig. 3(b)] with respect to the PL spectrum of $MAPbI_3$. The peak shift reaches a maximum for films with $a_{sol} = 3\%$ and decreases with higher concentrations of Mn^{2+}, at which the PL peak position is almost identical to that of $MAPbI_3$ [Fig. 3(c)]. The dependency is similar to what we observed in Figs. 2(b) and 2(c) for the XRD data, which strengthens the idea that for films with $a_{sol} > 3\%$ the Mn^{2+} is located in Mn-rich domains and not in the perovskite lattice.

Apart from the shift in the PL peak position, the TRPL lifetime [Fig. 3(d)] is influenced by the presence of Mn^{2+}. We performed mono-exponential fits on the TRPL traces (Fig. S3) and collected the TRPL lifetimes in Table SIII. The TRPL lifetime for the $MAPbI_3$ sample is 70 ns. For the film with $a_{sol} = 3\%$, the TRPL lifetime is a factor 2 larger (140 ns). This enhancement is in agreement with that measured in Ref. 19 by means of transient absorption experiments. On the contrary, the formation of Mn-rich domains causes a reduction in the TRPL lifetime. This occurs to some extent in the film with $a_{sol} = 10\%$ and becomes particularly evident for even higher Mn^{2+} concentrations. Furthermore, the PL emission of the film with $a_{sol} = 30\%$ is significantly quenched in comparison with the other samples (Fig. S4). These results indicate that for large Mn^{2+} concentrations non-radiative recombination pathways dominate the charge dynamics, which will be discussed in more detail below.

We further investigated the charge dynamics of light induced excess carriers by TRMC.[37] In short, photoexcitation of the film by means of a nano-second laser pulse at 550 nm results in the generation of free charges, which leads to an increase in the conductance of the sample. The photo-conductance (ΔG) is probed by measuring the reduction in reflected microwave power in time. After an initial rise corresponding to photogeneration of free charges, ΔG decays as a result of charge recombination and/or immobilization of charges in deep trap states. The TRMC traces have been corrected for the fraction of absorbed photons, Fa, which eliminates the effect of optical inhomogeneities.

Intensity-normalized TRMC traces are displayed in Figs. 4(a)–4(d) for films with different concentrations of Mn. For the film with $a_{sol} = 3\%$, the TRMC lifetimes are slightly longer [compare Fig. 4(a) with 4(b)], in line with the TRPL observations. However, for films with $a_{sol} > 3\%$, the charge carrier lifetimes drop significantly.

Hutter *et al.* modelled TRMC traces of MAPbI$_3$ films using a kinetic model representing a p-type semiconductor including band-to-band recombination and recombination via deep trap states [Fig. 4(e)].[38] The trapping process in this model is assumed to be a second-order process. More details about the method and the set of coupled differential equations which describe the time evolution of the populations of free and trapped charges are given in the supplementary material. We used the same model to reproduce the TRMC data presented in Figs. 4(a)–4(d). Note that this fully mathematical model also holds for the opposite situation, i.e., an n-type perovskite with trap states for holes and additional dark CB electrons.
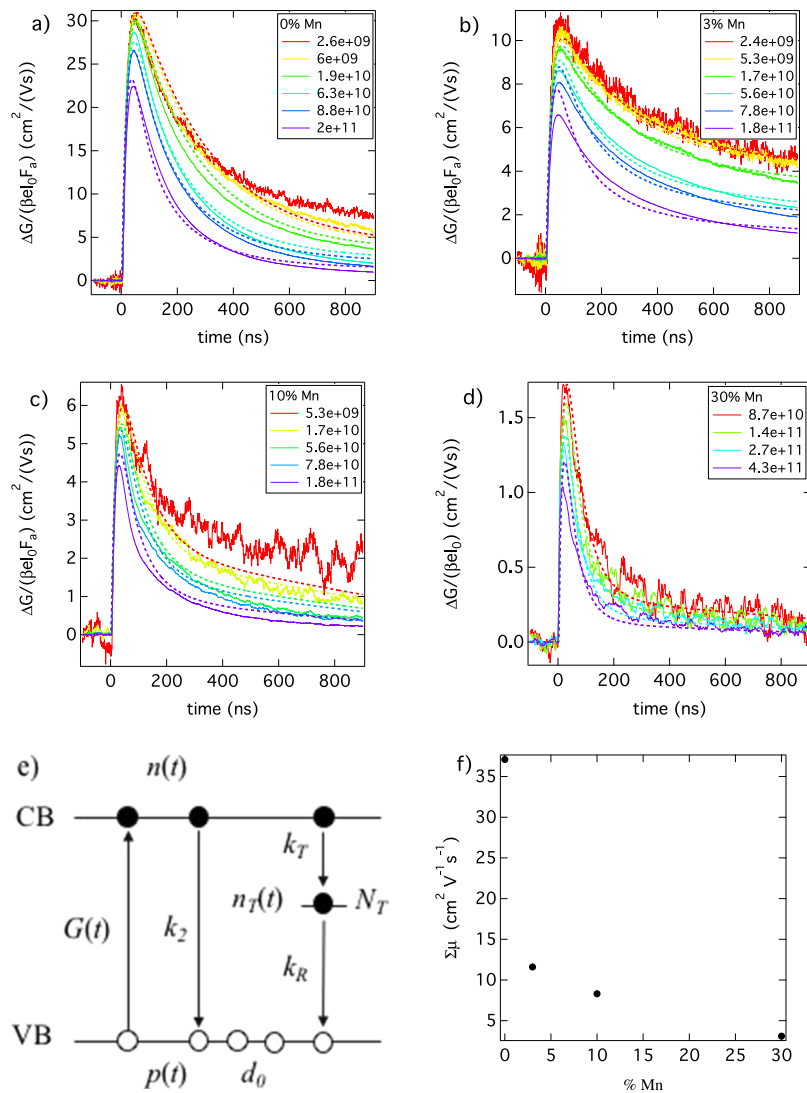
FIG. 4. [(a)–(d)] TRMC traces for mixed-metal perovskite thin films with different concentrations of Mn, recorded upon pulsed laser excitation at 550 nm at room temperature. The change in photoconductance, ΔG, is normalized for the number of incident photons I_0 and for the fraction of absorbed photons F_a. Solid lines represent experimental data, and dashed lines are calculated using the model presented in Ref. 38; (e) schematic representation of the kinetic model used for the modeling. The meaning of the symbols is reported in Table II; (f) sum of electron and hole mobilities, $\sum \mu$, as function of the percentage MnCl$_2$ in the precursor solution.

TABLE II. Parameters used for the modeling of the TRMC traces in Figs. 4(a)–4(d).

Parameter (units)	Description	0% Mn	3% Mn	10% Mn	30% Mn
$\mu_>$ (cm^2 V^{-1} s^{-1})	Majority carrier mobility	20.1	11.1	6.1	1.7
$\mu_<$ (cm^2 V^{-1} s^{-1})	Minority carrier mobility	17.0	0.5	2.1	1.4
$\mu_</\mu_>$ (–)	Mobility ratio	0.85	0.05	0.34	0.82
k_2 ($\times 10^{-10}$ cm^3 s^{-1})	Band-to-band recombination rate	6.9	6.4	7.2	15.0
k_T ($\times 10^{-10}$ cm^3 s^{-1})	Trap filling rate	1.5	3.6	6.0	7.0
k_R ($\times 10^{-11}$ cm^3 s^{-1})	Trap recombination rate	1.4	5.8	7.0	7.0
N_T ($\times 10^{15}$ cm^{-3})	Trap density	5.4	5.5	6.0	5.5
d_0 ($\times 10^{15}$ cm^{-3})	Background density	4.2	3.5	9.0	7.0

Using the parameters listed in Table II, the model reproduces the experimental trends fairly well [dashed lines in Figs. 4(a)–4(d)]. We note that for MAPbI$_3$ without Mn^{2+} we obtain similar kinetic values as reported earlier.[38] The film with a_{sol} = 3% is characterized by a slightly smaller k_2 as compared to MAPbI$_3$. This is well in line with the longer TRPL lifetime found for this sample. In addition, the presence of Mn^{2+} in the perovskite lattice has a large effect on the mobilities of both charges, which become greatly unbalanced. We note here that the TRMC does not allow distinguishing between electrons and holes since mobile carriers interact with the microwave radiation independently on the sign of their charge. Nevertheless, the kinetic model reported in the supplementary material makes a distinction between the majority and the minority charges. In order to reproduce the TRMC data for the sample with a_{sol} = 3%, we have to set the mobility of majority charges one order of magnitude larger than the mobility of minority charges.

The formation of Mn-rich domains for films with a_{sol} > 3% leads to faster decay kinetics, which translates into an increase in k_2. In addition, the TRMC data clearly show that alloying Mn^{2+} in MAPbI$_3$ negatively affects the mobilities. Figure 4(f) shows the sum of electron and hole mobilities, $\sum\mu$, used to calculate the TRMC traces in Figs. 4(a)–4(d). For the film with a_{sol} = 3%, a reduction of $\sum\mu$ by a factor 3 is found. With higher concentrations of Mn^{2+}, an additional reduction in mobility, in combination with an increase in the trap density, trap filling, and trap recombination rate constants are observed.

To verify how the presence of Mn^{2+} changes the charge dynamics for electron and holes, we carried out DFT calculations including spin-orbit coupling to reveal the band structure of MAPbI$_3$, MAPb$_{0.9375}$Mn$_{0.0625}$I$_3$, and MAPb$_{0.875}$Mn$_{0.125}$I$_3$ (Fig. 5). The choice of these compositions is motivated by the computational constrains of the DFT simulations. We have calculated the effective masses of electrons and holes, listed in Table III by using the parabolic fitting method. The effective masses of MAPbI$_3$ are in good agreement with reported theoretical studies.[39,40] Interestingly, the curvature of the valence band (VB) of MAPb$_{0.9375}$Mn$_{0.0625}$I$_3$ is much wider than the curvature of the conduction band (CB) due to interaction of Mn with the rest of the Pb$_{1-a}$I$_3$ lattice (hybridization
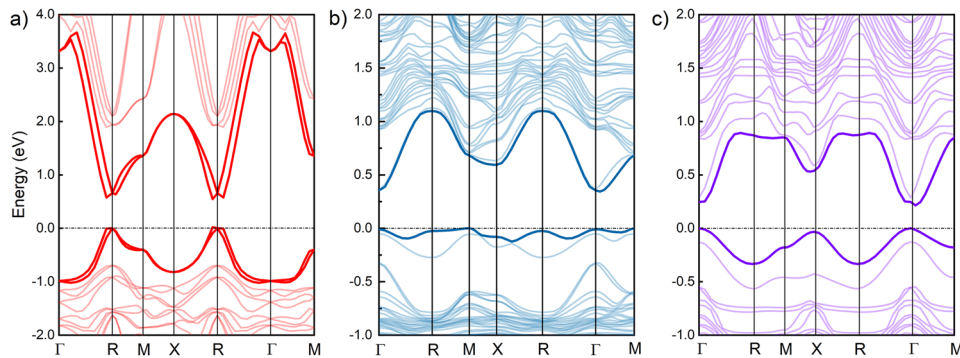

FIG. 5. Band structure (VBM and CBM in bold) of cubic (a) MAPbI$_3$, (b) MAPb$_{0.9375}$Mn$_{0.0625}$I$_3$, and (c) MAPb$_{0.875}$Mn$_{0.125}$I$_3$ as calculated by DFT with spin orbit coupling.

TABLE III. Calculated effective masses of electrons and holes expressed in units of the free-electron mass, (m_0) for MAPbI$_3$, MAPb$_{0.9375}$Mn$_{0.0625}$I$_3$, and MAPb$_{0.875}$Mn$_{0.125}$I$_3$.

	m_n^*	m_p^*	m_p^*/m_n^*	m_n^*	m_p^*	m_p^*/m_n^*
MAPbI$_3$	0.23 (R-Γ)	0.25 (R-Γ)	1.09	0.33 (R-M)	0.51 (R-M)	1.55
MAPb$_{0.9375}$Mn$_{0.0625}$I$_3$	0.25 (Γ-M)	2.79 (Γ-M)	11.16	0.35 (Γ-R)	1.37 (Γ-R)	3.91
MAPb$_{0.875}$Mn$_{0.125}$I$_3$	0.51 (Γ-R)	1.10 (Γ-R)	2.16	0.68 (Γ-M)	2.16 (Γ-M)	3.18

of s and d states of Mn with s state of Pb and p state of I). This means that the effective mass of the holes is much larger than the effective mass of the electrons (Table III), and hence the electrons are more mobile than holes. Another interesting point to note is that the effective mass of holes of the MAPb$_{0.9375}$Mn$_{0.0625}$I$_3$ is significantly larger than that of MAPbI$_3$, while the effective mass of the electrons is similar in the two samples. Given the effective masses calculated by DFT, we argue that the electrons in the mixed metal perovskite have a substantial larger mobility than the holes. Combining TRMC and DFT allows us to conclude that, in the sample with a_{sol} = 3%, the electrons are the majority carriers and that therefore the material is most likely n-type. For samples with a larger concentration of Mn^{2+}, we keep the assumption of the n-type material.

The effective masses of electrons and holes in MAPb$_{0.875}$Mn$_{0.125}$I$_3$ are larger than those of MAPbI$_3$. This is in agreement with the incorporation of a transition metal, such as Ag, Cu, or Au in MA$_2$BB′I$_6$ (B and B′ are metal cations). The corresponding effective masses are generally larger than those of lead halide perovskites.[41] However, in view of the XRD data previously shown and the conclusions about the segregation of Mn^{2+} out of the perovskite structure for films with a_{sol} > 3%, we do not consider the calculated DFT effective masses of MAPb$_{0.875}$Mn$_{0.125}$I$_3$ to be related to the lower TRMC mobilities observed in Figs. 4(c) and 4(d). Instead, at higher Mn^{2+} concentrations, it seems likely that the reduction in $\sum \mu$ is, at least partially, caused by a reduction in the size of crystalline domains in the film and the formation of more grain boundaries that would slow down the motion of free charges. Secondary electron SEM images (Fig. S5) show that the perovskite crystalline domains are smaller for the film with a_{sol} = 30% than those for the film with a_{sol} = 10%. Thus, the change in domain size is likely to lead to a reduction in the charge mobilities when the Mn^{2+} concentration is increased from a_{sol} = 10% to a_{sol} = 30%. In addition, the amorphous Mn^{2+} rich phases formed in films with a_{sol} > 10% are expected to enhance to charge decay as observed in the TRPL and TRMC measurements.

In this work, we partially replaced Pb^{2+} with Mn^{2+} in MAPbI$_3$ and studied the change in structural and electronic properties of the resulting films. From structural and elemental analysis, we conclude that only a limited amount of the Pb^{2+} atoms at the B position of the perovskite structure can be replaced by Mn^{2+}. Using precursor solutions with higher Mn^{2+} concentrations leads to the formation of additional amorphous Mn-rich domains. At 3% replacement, the band-to-band recombination rate slightly reduces yielding somewhat longer charge carrier lifetimes as determined from TRPL and TRMC measurements. However, this is accompanied by a substantial increase in the effective mass of the holes, resulting in a strongly unbalanced charge transport. According to the recent results of Zheng *et al.*, the increase in charge carrier lifetimes still positively affects the photovoltaic performance of devices made from this composition.[19] For higher concentrations of Mn^{2+}, formation of Mn-rich domains restores the balanced transport, although both electron mobility and hole mobility become ca. 1 order of magnitude smaller than in MAPbI$_3$ due to enhanced charge scattering. Besides the lowering of the mobilities, a reduction in the charge lifetime is found. At higher concentrations of Mn^{2+}, the reduced charge carrier diffusion lengths will be severely limiting the photovoltaic properties of solar cells prepared from these mixed metal halide perovskites. These findings are in line with the lower efficiencies observed in MAPbI$_3$ solar cells in which more than 5% of the Pb^{2+} was replaced by Mn^{2+}.[18,19] Combination of experimental and theoretical data indicates that alloying MAPbI$_3$ with small amounts of Mn^{2+} is a unique handle to manipulate the dynamics of the carriers.

See supplementary material for the differential equations used for modeling the TRMC data and for additional data.

[1] A. Kojima, K. Teshima, Y. Shirai, and T. Miyasaka, "Organometal halide perovskites as visible-light sensitizers for photovoltaic cells," J. Am. Chem. Soc. **131**(17), 6050–6051 (2009).

[2] J.-P. Correa-Baena, A. Abate, M. Saliba, W. Tress, T. Jesper Jacobsson, M. Gratzel, and A. Hagfeldt, "The rapid evolution of highly efficient perovskite solar cells," Energy Environ. Sci. **10**(3), 710–727 (2017).

[3] J. A. Christians, P. Schulz, J. S. Tinkham, T. H. Schloemer, S. P. Harvey, B. J. Tremolet de Villers, A. Sellinger, J. J. Berry, and J. M. Luther, "Tailored interfaces of unencapsulated perovskite solar cells for >1000 hour operational stability," Nat. Energy **3**(1), 68–74 (2018).

[4] H.-S. Kim, C.-R. Lee, J.-H. Im, K.-B. Lee, T. Moehl, A. Marchioro, S.-J. Moon, R. Humphry-Baker, J.-H. Yum, J. E. Moser *et al.*, "Lead iodide perovskite sensitized all-solid-state submicron thin film mesoscopic solar cell with efficiency exceeding 9%," Sci. Rep. **2**, 591 (2012).

[5] M. M. Lee, J. Teuscher, T. Miyasaka, T. N. Murakami, and H. J. Snaith, "Efficient hybrid solar cells based on meso-superstructured organometal halide perovskites," Science **338**, 643 (2012).

[6] N. J. Jeon, J. H. Noh, Y. C. Kim, W. S. Yang, S. Ryu, and S. Seok Il, "Solvent engineering for high-performance inorganic–organic hybrid perovskite solar cells," Nat. Mater. **13**, 897 (2014).

[7] N. J. Jeon, J. H. Noh, W. S. Yang, Y. C. Kim, S. Ryu, J. Seo, and S. Seok Il, "Compositional engineering of perovskite materials for high-performance solar cells," Nature **517**, 476 (2015).

[8] J. Albero, A. M. Asiri, and H. Garcia, "Influence of the composition of hybrid perovskites on their performance in solar cells," J. Mater. Chem. A **4**(12), 4353–4364 (2016).

[9] L. Atourki, E. Vega, B. Marí, M. Mollar, H. Ait Ahsaine, K. Bouabid, and A. Ihlal, "Role of the chemical substitution on the structural and luminescence properties of the mixed halide perovskite thin MAPbI3−xBrx (0 ≤ x ≤ 1) films," Appl. Surf. Sci. **371**, 112–117 (2016).

[10] M. Saliba, T. Matsui, K. Domanski, J.-Y. Seo, A. Ummadisingu, S. M. Zakeeruddin, J.-P. Correa-Baena, W. R. Tress, A. Abate, A. Hagfeldt *et al.*, "Incorporation of rubidium cations into perovskite solar cells improves photovoltaic performance," Science **354**(6309), 206–209 (2016).

[11] Z. Fan, S. T. Williams, L. Po-Wei, C. Chu-Chen, L. Chien-Yi, and A. K.-Y. Jen, "Binary-metal perovskites toward high-performance planar-heterojunction hybrid solar cells," Adv. Mater. **26**(37), 6454–6460 (2014).

[12] G. E. Eperon and D. S. Ginger, "B-site metal cation exchange in halide perovskites," ACS Energy Lett. **2**(5), 1190–1196 (2017).

[13] F. Hao, C. C. Stoumpos, R. P. H. Chang, and M. G. Kanatzidis, "Anomalous band gap behavior in mixed Sn and Pb perovskites enables broadening of absorption spectrum in solar cells," J. Am. Chem. Soc. **136**(22), 8094–8099 (2014).

[14] A. Babayigit, A. Ethirajan, M. Muller, and B. Conings, "Toxicity of organometal halide perovskite solar cells," Nat. Mater. **15**, 247 (2016).

[15] D. Zhao, Y. Yu, C. Wang, W. Liao, N. Shrestha, C. R. Grice, A. J. Cimaroli, L. Guan, R. J. Ellingson, K. Zhu *et al.*, "Low-bandgap mixed tin–lead iodide perovskite absorbers with long carrier lifetimes for all-perovskite tandem solar cells," Nat. Energy **2**, 17018 (2017).

[16] N. K. Noel, S. D. Stranks, A. Abate, C. Wehrenfennig, S. Guarnera, A.-A. Haghighirad, A. Sadhanala, G. E. Eperon, S. K. Pathak, M. B. Johnston *et al.*, "Lead-free organic-inorganic tin halide perovskites for photovoltaic applications," Energy Environ. Sci. **7**(9), 3061–3068 (2014).

[17] T. Leijtens, R. Prasanna, A. Gold-Parker, M. F. Toney, and M. D. McGehee, "Mechanism of tin oxidation and stabilization by lead substitution in tin halide perovskites," ACS Energy Lett. **2**(9), 2159–2165 (2017).

[18] M. T. Klug, A. Osherov, A. A. Haghighirad, S. D. Stranks, P. R. Brown, S. Bai, J. T.-W. Wang, X. Dang, V. Bulovic, H. J. Snaith *et al.*, "Tailoring metal halide perovskites through metal substitution: Influence on photovoltaic and material properties," Energy Environ. Sci. **10**(1), 236–246 (2017).

[19] H. Zheng, G. Liu, X. Xu, A. Alsaedi, T. Hayat, X. Pan, and S. Dai, "Acquiring high-performance and stable mixed-dimensional perovskite solar cells by using transition metal substituted Pb," ChemSusChem **11**(18), 3269 (2018).

[20] See https://www.atsdr.cdc.gov/toxprofiles/tp151-c2.pdf for Background and Environmental Exposures to Manganese in the United States.

[21] P. Singh, P. J. S. Rana, P. Dhingra, and P. Kar, "Towards toxicity removal in lead based perovskite solar cells by compositional gradient using manganese chloride," J. Mater. Chem. C **4**(15), 3101–3105 (2016).

[22] B. Náfrádi, P. Szirmai, M. Spina, H. Lee, O. V. Yazyev, A. Arakcheeva, D. Chernyshov, M. Gibert, L. Forró, and E. Horváth, "Optically switched magnetism in photovoltaic perovskite $CH_3NH_3(Mn:Pb)I_3$," Nat. Commun. **7**, 13406 (2016).

[23] D. Parobek, B. J. Roman, Y. Dong, H. Jin, E. Lee, M. Sheldon, and D. H. Son, "Exciton-to-dopant energy transfer in Mn-doped cesium lead halide perovskite nanocrystals," Nano Lett. **16**(12), 7376–7380 (2016).

[24] S. Zou, Y. Liu, J. Li, C. Liu, R. Feng, F. Jiang, Y. Li, J. Song, H. Zeng, M. Hong *et al.*, "Stabilizing cesium lead halide perovskite lattice through Mn(II) substitution for air-stable light-emitting diodes," J. Am. Chem. Soc. **139**(33), 11443–11450 (2017).

[25] W. J. Mir, M. Jagadeeswararao, S. Das, and A. Nag, "Colloidal Mn-doped cesium lead halide perovskite nanoplatelets," ACS Energy Lett. **2**(3), 537–543 (2017).

[26] J. P. Perdew, K. Burke, and M. Ernzerhof, "Generalized gradient approximation made simple," Phys. Rev. Lett. **77**(18), 3865–3868 (1996).

[27] G. Kresse and J. Furthmüller, "Efficiency of *ab-initio* total energy calculations for metals and semiconductors using a plane-wave basis set," Comput. Mater. Sci. **6**(1), 15–50 (1996).

[28] G. Kresse and J. Furthmüller, "Efficient iterative schemes for *ab initio* total-energy calculations using a plane-wave basis set," Phys. Rev. B **54**(16), 11169–11186 (1996).

[29] P. E. Blöchl, "Projector augmented-wave method," Phys. Rev. B **50**(24), 17953–17979 (1994).

[30] G. Kresse and D. Joubert, "From ultrasoft pseudopotentials to the projector augmented-wave method," Phys. Rev. B **59**(3), 1758–1775 (1999).

[31] X. Zhang, J. Yin, Z. Nie, Q. Zhang, N. Sui, B. Chen, Y. Zhang, K. Qu, J. Zhao, and H. Zhou, "Lead-free and amorphous organic-inorganic hybrid materials for photovoltaic applications: Mesoscopic $CH_3NH_3MnI_3/TiO_2$ heterojunction," RSC Adv. **7**(59), 37419–37425 (2017).

[32] V. M. Goldschmidt, "Die gesetze der krystallochemie," Naturwissenschaften **14**, 477–485 (1926).

[33] W. Travis, E. N. K. Glover, H. Bronstein, D. O. Scanlon, and R. G. Palgrave, "On the application of the tolerance factor to inorganic and hybrid halide perovskites: A revised system," Chem. Sci. **7**(7), 4548–4556 (2016).

[34] C. Li, X. Lu, W. Ding, L. Feng, Y. Gao, and Z. Guo, "Formability of ABX3 (X = F, Cl, Br, I) halide perovskites," Acta Crystallogr., Sect. B **64**(6), 702–707 (2008).

[35] Q. Wang, M. Lyu, M. Zhang, J.-H. Yun, H. Chen, and L. Wang, "Transition from the tetragonal to cubic phase of organohalide perovskite: The role of chlorine in crystal formation of $CH_3NH_3PbI_3$ on TiO_2 substrates," J. Phys. Chem. Lett. **6**(21), 4379–4384 (2015).

[36] D. Bai, J. Zhang, Z. Jin, H. Bian, K. Wang, H. Wang, L. Liang, Q. Wang, and S. F. Liu, "Interstitial Mn^{2+}-driven high-aspect-ratio grain growth for low-trap-density microcrystalline films for record efficiency $CsPbI_2Br$ solar cells," ACS Energy Lett. **3**(4), 970–978 (2018).

[37] T. J. Savenije, A. J. Ferguson, N. Kopidakis, and G. Rumbles, "Revealing the dynamics of charge carriers in polymer:fullerene blends using photoinduced time-resolved microwave conductivity," J. Phys. Chem. C **117**(46), 24085–24103 (2013).

[38] E. M. Hutter, G. E. Eperon, S. D. Stranks, and T. J. Savenije, "Charge carriers in planar and meso-structured organic–inorganic perovskites: Mobilities, lifetimes, and concentrations of trap states," J. Phys. Chem. Lett. **6**(15), 3082–3090 (2015).

[39] G. Giorgi, J.-I. Fujisawa, H. Segawa, and K. Yamashita, "Small photocarrier effective masses featuring ambipolar transport in methylammonium lead iodide perovskite: A density functional analysis," J. Phys. Chem. Lett. **4**(24), 4213–4216 (2013).

[40] P. Umari, E. Mosconi, and F. De Angelis, "Relativistic GW calculations on $CH_3NH_3PbI_3$ and $CH_3NH_3SnI_3$ perovskites for solar cell applications," Sci. Rep. **4**, 4467 (2014).

[41] T. Nakajima and K. Sawada, "Discovery of Pb-free perovskite solar cells via high-throughput simulation on the K computer," J. Phys. Chem. Lett. **8**(19), 4826–4831 (2017).